Comput. Methods Appl. Mech. Engrg. 247–248 (2012) 51–64

Contents lists available at SciVerse ScienceDirect

Comput. Methods Appl. Mech. Engrg.

journal homepage: www.elsevier.com/locate/cma

On continuum immersed strategies for Fluid–Structure Interaction

C. Hesch *, A.J. Gil, A. Arranz Carreño, J. Bonet

Chair of Computational Mechanics, Department of Mechanical Engineering, University of Siegen, Germany
Civil and Computational Engineering Centre, College of Engineering, Swansea University, Singleton Park, Swansea SA2 8PP, United Kingdom

ARTICLE INFO

Article history:
Received 1 April 2012
Received in revised form 22 July 2012
Accepted 31 July 2012
Available online 11 August 2012

Keywords:
IFEM
ISPM
Fluid–Structure Interaction
Structure preserving time integration
Isogeometric analysis

ABSTRACT

Continuum immersed strategies are widely used these days for the computational simulation of Fluid–Structure Interaction problems. The principal characteristic of such immersed techniques is the representation of the immersed solid via a momentum forcing source in the Navier–Stokes equations. In this paper, the Immersed Finite Element Method (IFEM), introduced by Zhang et al. (2004) [41] for the analysis of deformable solids immersed in an incompressible Newtonian viscous fluid, is further enhanced by means of three new improvements. A first update deals with the modification of the conservation of mass equation in the background fluid in order to account for non-isochoric deformations within the solid phase. A second update deals with the incompressibility constraint for the solid phase in the case of isochoric deformations, where an enhanced evaluation of the deformation gradient tensor is introduced in a multifield Hu-Washizu variational sense in order to overcome locking effects. The third update is focussed on the improvement of the robustness of the overall scheme, by introducing an implicit one-step time integration scheme with enhanced stability properties, in conjunction with a consistent Newton–Raphson linearisation strategy for optimal quadratic convergence. The resulting monolithic methodology is thoroughly studied for a range of Lagrangian and NURBS based shape finite element functions for a series of numerical examples, with the purpose of studying the effect of the spatial semi-discretisation in the solution. Comparisons are also established with the newly developed Immersed Structural Potential Method (ISPM) by Gil et al. (2010) [7] for benchmarking and assessment of the quality of the new formulation.

1. Introduction

The computational analysis of Fluid–Structure Interaction (FSI) phenomena is widely used these days for a wealth of industrial and physical applications. In particular, the field of biomechanics has observed a surge over the last decade in the application of these computational techniques for the modelling of biological tissues (i.e. heart valves) interacting with biological fluids (i.e. blood). Some of these problems are highly challenging, requiring the modelling of highly deformable solids immersed within a surrounding incompressible Newtonian viscous fluid. In this case, a stable and robust computational algorithm becomes essential for a successful simulation.

Partitioned boundary-fitted methods are a well established strategy for the modelling of FSI effects or more general coupled multifield problems. These methods are usually based upon an Arbitrary Lagrangian Eulerian approach [5]. Monolithic strongly coupled Dirichlet–Neumann schemes as proposed in [33] or partitioned staggered alternatives as in [38], require the spatial discretisation of the interface to transfer information between the interacting phases. Sophisticated discretisation schemes, like the dual mortar method recently introduced in [18], have been designed to optimise the transfer of momentum between the different phases. The modelling of the interface can also be carried out by means of the eXtended Finite Element Method (XFEM) [6]. One disadvantage in the above boundary-fitted approaches stems from the necessity to resort to moving/remeshing algorithms to update the referential fluid mesh, which can turn to be computationally expensive in terms of the overall algorithm [21].

An alternative group of FSI methodologies are based upon the Immersed Boundary Method (IBM) pioneered by Peskin [25–27]. This method relies on the representation of the solid–fluid interface as a momentum forcing source in the Navier–Stokes equations governing the behaviour of the fluid. The force term was initially included to represent the effect of an immersed thin solid structure (i.e. heart valve) modelled as an assemblage of curvilinear Lagrangian fibre-like elements in an incompressible viscous fluid (i.e. blood stream). This approach was later improved and extended in the form of the Immersed Finite Element Method (IFEM) by Zhang and Liu [41,36,35], to suitably analyse continuum immersed solids (for compressible fluids see Wang et al. [37]). In this approach, the

* Corresponding author at: Chair of Computational Mechanics, Department of Mechanical Engineering, University of Siegen, Germany. Tel.: +49 271 740 2101; fax: +49 271 740 2436.
E-mail address: christian.hesch@uni-siegen.de (C. Hesch).

0045-7825/$ - see front matter © 2012 Elsevier B.V. All rights reserved.
http://dx.doi.org/10.1016/j.cma.2012.07.021

immersed solid is discretised in space following a Finite Element approach, requiring the generation of a computational mesh. Recently, in Gil et al. [7,8], the authors introduced the definition of a deviatoric strain energy functional to characterise the behaviour of the immersed structure, where its spatial gradient defines the FSI force field, resulting in the so-called Immersed Structural Potential Method (ISPM). In this case, the solid is modelled as a collection of integration points (i.e. quadrature points), removing the need for an initial computational mesh. All in all, these immersed methodologies have been proven to be computationally very efficient and competitive with numerous applications in biomedical FSI problems [19].

In continuum immersed strategies, the background fluid is modelled using a standard Eulerian description, whilst the immersed solid is described in a Lagrangian manner. The introduction of an Euler–Lagrange mapping operator, which enables the transfer of information between both descriptions [31], is crucial to the success of these approaches. In this sense, the discretisation approach employed for the fluid, solid and the Euler–Lagrange mapping will be demonstrated to have clear effects in the numerical solution.

In this paper, the incompressible Newtonian fluid is resolved following a standard Finite Element semi-discretisation method [5] with isoparametric quadrilateral elements. The effect of both classical Lagrange and more recent NURBS based shape functions [15,16,9,22] will be explored. Regarding the former, a Q2Q1 Taylor–Hood element and a lower order Q1Q1 element will be implemented and compared. It is well known that since the Q1Q1 element does not satisfy the LBB condition (see [5,14,32,34]), the Streamline Upwind Petrov Galerkin (SUPG) method must be employed for stabilisation.

The immersed solid is modelled following both the IFEM and ISPM approaches in order to further assess their feasibility and range of application. For the modelling of the solid, both compressible and nearly incompressible scenarios will be studied. To account for compressible immersed solids, the conservation of mass equation in the background fluid domain will be suitably modified to take into consideration the presence of a volumetric deformation. In the incompressibility limit, the IFEM approach, based on a Finite Element discretisation of the solid phase, suffers from well reported locking effects [1]. A solution to this deficiency, based on the use of enhanced elements (see [30,28,29]), will be implemented and tested.

For the time-integration of the resulting semi-discrete system, a monolithic, consistent and fully implicit time integration scheme will be employed for both the fluid and the immersed solid. Structure preserving integrators are well known within the context of non-linear elastodynamics (see [23,24,10]). These algorithms can be straightforwardly applied without any further modification, resulting in highly stable schemes enabling the use of very large time steps with optimum dissipation/dispersion properties.

This paper is broken down into the following sections. In Section 2, the governing partial differential equations (strong form) of the problem are presented for both the fluid and solid phases and are further elaborated into a variational format (weak form) for subsequent numerical analysis. An important aspect relating to the modification of the conservation of mass equation in the background fluid field is presented with the purpose of accounting for volumetric deformations in the solid phase. Section 3 focusses on various possible finite element based spatial discretisation strategies (i.e. Lagrangian or NURBS based) used to resolve the underlying equations. In this section, the Euler–Lagrange discrete mapping operator is described in depth, highlighting the existing differences between the various IFEM formulations and the ISPM approach. In Section 4, the time discretisation strategy is presented for both the fluid, solid and the Euler–Lagrange operator. Section 5 displays an extensive range of numerical examples in order to demonstrate the flexibility and robustness of the formulation, drawing key comparisons between the various competing approaches. Finally, in Section 6, some concluding remarks will be drawn.

2. Problem formulation

The objective of this section is to provide a brief outline of the fundamental equations governing the problem under consideration. Subsections one and two summarise the standard formulation of the Newtonian viscous fluid system described by the incompressible Navier–Stokes equations. We refer to the seminal works by Donea and Huerta [5] and Zienkiewicz et al. [42] for a detailed analysis of this topic. Subsections three and four focus on the mathematical description of the immersed deformable solid phase following the pioneering work of Peskin [25,27] and the subsequent extension to a continuum medium introduced by Zhang et al. [41].

2.1. Fluid system – strong formulation

We consider a single bounded domain $\Omega \subset \mathbb{R}^d,\ d \in [2,3]$. The material position of a particle is labelled by $\boldsymbol{X}$ whereas the actual position is labelled by $\boldsymbol{x}$. Both positions are linked during the time interval of interest $t \in \mathbb{I} = [0,T]$ by the deformation mapping $\boldsymbol{\varphi} : \Omega \times [0,T] \to \mathbb{R}^d$ such that $\boldsymbol{x}(t) = \boldsymbol{\varphi}(\boldsymbol{X},t)$. As usual, we write the fluid system in terms of an Eulerian description using the inverse mapping $\boldsymbol{X} = \boldsymbol{\varphi}^{-1}(\boldsymbol{x}(t),t)$. For the time differential of a physical quantity $f(\boldsymbol{x}(t),t)$, it follows immediately that

$$\dot{f} = \frac{\partial f}{\partial t} + \boldsymbol{v} \cdot \nabla_{\boldsymbol{x}} f, \tag{1}$$

where $\boldsymbol{v}(\boldsymbol{x}(t),t) = \partial\boldsymbol{\varphi}/\partial t$ denotes the velocity at a specific point. Without loss of generality we restrict ourselves to the incompressible case and obtain for the conservation of mass equation

$$\nabla_{\boldsymbol{x}} \cdot \boldsymbol{v} = \frac{\dot{J}}{J} \equiv 0, \tag{2}$$

where $J = \det(\boldsymbol{F})$ and $\boldsymbol{F} : \Omega \times [0,T] \to \mathbb{R}^{d\times d},\ \boldsymbol{F} = D\boldsymbol{\varphi}$ denotes the deformation gradient tensor. For a Newtonian viscous fluid the Cauchy stress tensor $\boldsymbol{\sigma} : \Omega \times [0,T] \to \mathbb{R}^{d\times d}$ is defined by

$$\boldsymbol{\sigma} = -p\boldsymbol{I} + \lambda \nabla_{\boldsymbol{x}} \cdot \boldsymbol{v} + \mu\left(\nabla_{\boldsymbol{x}}\boldsymbol{v} + \nabla_{\boldsymbol{x}}\boldsymbol{v}^T\right), \tag{3}$$

where μ denotes the dynamic viscosity and λ the second coefficient of viscosity. Here, the pressure $p : \Omega \times [0,T] \to \mathbb{R}$ is a sufficiently smooth function and can be regarded as a Lagrange multiplier introduced to enforce condition (2). Note that for the case of an incompressible fluid the second term on the right hand side vanishes. The non-conservative Eulerian form of the balance of linear momentum reads,

$$\rho\dot{\boldsymbol{v}} = \nabla_{\boldsymbol{x}} \cdot \boldsymbol{\sigma} + \rho\boldsymbol{g}, \tag{4}$$

where ρ denotes the density and $\boldsymbol{g}$ a prescribed body force per unit of mass. Finally, suitable boundary conditions need to be introduced on the boundary Γ of the domain Ω as follows,

$$\begin{aligned} &\boldsymbol{v} = \boldsymbol{u}, \quad \text{on } \Gamma^u \times [0,T], \\ &\boldsymbol{\sigma} \cdot \boldsymbol{n} = \boldsymbol{h}, \quad \text{on } \Gamma^h \times [0,T]. \end{aligned} \tag{5}$$

Here, $(5)_1$ and $(5)_2$ denote the Dirichlet and Neumann boundary conditions, respectively, with $\Gamma^u \cup \Gamma^h = \Gamma,\ \Gamma^u \cap \Gamma^h = \emptyset$ and $\boldsymbol{n}$ the outward unit normal vector.

2.2. Fluid system – weak formulation

Following a standard variational formulation, we recast the above system of partial differential equations (strong form) in its variational counterpart (weak form). Hence, suitable functional spaces of test functions for both the velocity and pressure fields are introduced as follows,

$$\begin{aligned}\mathbb{V}^v &=: \{\delta\boldsymbol{v} \in \mathbb{H}^1(\Omega) | \delta\boldsymbol{v} = \boldsymbol{0} \text{ on } \Gamma^u\},\\ \mathbb{V}^p &=: \{\delta p \in L_2(\Omega)\},\end{aligned} \tag{6}$$

where the Sobolev functional space $\mathbb{H}^1$ contains the set of square integrable functions with square integrable spatial gradient. Setting the inner product in Ω and its boundary $\partial\Omega$ in the usual fashion,

$$\int_\Omega (\bullet)\cdot(\bullet)\mathrm{d}v =: \langle \bullet, \bullet\rangle \quad \text{and} \quad \int_{\partial\Omega} (\bullet)\cdot(\bullet)\mathrm{d}a =: \langle \bullet, \bullet\rangle_\Gamma \tag{7}$$

we can rewrite the balance of linear momentum as follows,

$$\langle \rho(\dot{\boldsymbol{v}} - \boldsymbol{g}), \delta\boldsymbol{v}\rangle + \langle \boldsymbol{\sigma}, \nabla_{\boldsymbol{x}}(\delta\boldsymbol{v})\rangle - \langle \boldsymbol{h}, \delta\boldsymbol{v}\rangle_{\Gamma^h} = 0 \tag{8}$$

supplemented by the kinematic constraint

$$\langle \nabla_{\boldsymbol{x}}\cdot\boldsymbol{v}, \delta p\rangle = 0. \tag{9}$$

Both Eqs. (8) and (9) have to hold for all $\delta\boldsymbol{v} \in \mathbb{V}^v$ and $\delta p \in \mathbb{V}^p$ for all times $t \in \mathbb{I} = [0, T]$.

2.3. Immersed solid system – strong formulation

Let us consider a deformable solid fully immersed within the surrounding incompressible viscous fluid. For the calculation of the Fluid–Structure Interaction (FSI) effect, an immersed continuum numerical strategy will be followed, where the deformable solid phase is modelled as embedded into the background fluid phase (see [20]). The resulting FSI forces are formulated in terms of a volumetric force field $\boldsymbol{\mathcal{F}} : \Omega_t^s \times [0, T] \to \mathbb{R}^d$ which emanates from the interaction of the background fluid system defined by the domain Ω with the immersed solid system defined by the domain Ω_t^s at time t. In Gil et al. [7,8], the authors model the solid as a Helmholtz's free energy functional whose spatial gradient defines the FSI force field. This force vector field $\boldsymbol{\mathcal{F}}$ can be introduced with no difficulty within the conservation of linear momentum of the background fluid phase in Eq. (4) as follows,[1]

$$\rho^f\dot{\boldsymbol{v}} = \nabla_{\boldsymbol{x}}\cdot\boldsymbol{\sigma}^f + \rho^f\boldsymbol{g} + \boldsymbol{\mathcal{F}}. \tag{10}$$

The volumetric force field $\boldsymbol{\mathcal{F}}$ of the immersed solid reads,

$$\boldsymbol{\mathcal{F}} = \begin{cases} \boldsymbol{0} & \text{in } \Omega\backslash\Omega_t^s,\\ (\rho^f - \rho^s)(\dot{\boldsymbol{v}} - \boldsymbol{g}) + \nabla\cdot(\boldsymbol{\sigma}^s - \boldsymbol{\sigma}^f) & \text{in } \Omega_t^s.\end{cases} \tag{11}$$

In addition, the conservation of mass Eq. (2) is modified allowing for the immersed solid to possibly experience non-isochoric deformations within the surrounding incompressible fluid, resulting in

$$\nabla_{\boldsymbol{x}}\cdot\boldsymbol{v} = \mathcal{F}^p, \tag{12}$$

where the scalar field $\mathcal{F}^p : \Omega_t^s \times [0, T] \to \mathbb{R}$ is defined as,

$$\mathcal{F}^p = \begin{cases} 0 & \text{in } \Omega\backslash\Omega_t^s,\\ \frac{\dot{J}}{J} & \text{in } \Omega_t^s.\end{cases} \tag{13}$$

Note that we do not need to introduce additional pressure unknowns for the solid, if it is assumed to be incompressible. Within the context of Green elastic materials [13], we next postulate the existence of a hyperelastic constitutive law for the calculation of the solid stress field by introducing a scalar valued stored strain energy functional $W(\boldsymbol{C})$, where $\boldsymbol{C} = \boldsymbol{F}^T\boldsymbol{F}$ denotes the right Cauchy–Green tensor. In general, additional internal thermodynamic variables can also be used to further characterise the constitutive law of the immersed solid (i.e. including plastic or viscoelastic behaviour). Moreover, in the case of nearly incompressible materials, sophisticated mixed formulations based upon the use of enhanced modes can also be utilised (see Appendix A for further details). The actual stress field of the immersed solid can be obtained via a push forward operation of the purely material derivative of the stored strain energy functional as,

$$\boldsymbol{\sigma}^s = \frac{2}{J}\boldsymbol{F}\frac{\partial W(\boldsymbol{C})}{\partial\boldsymbol{C}}\boldsymbol{F}^T. \tag{14}$$

For numerical convenience, it is customary to employ a Lagrangian mapping for the description of the immersed solid whilst the fluid is modelled by means of an Eulerian mapping. The kinematic information in terms of velocity and spatial position can easily be measured in the Eulerian background fluid and must be suitably linked to the solid phase in a compatible fashion (i.e. non-slip condition). Computations within the solid phase require then the definition of an Euler–Lagrange mapping $\mathcal{I}_{\Omega_t^s}$ for any given function ψ of the solid system such that $\psi(\boldsymbol{x}, t) : \Omega_t^s \times [0, T]$ is mapped to $\mathcal{I}_{\Omega_t^s}(\psi(\boldsymbol{X}, t)) : \Omega_0^s \times [0, T]$. In the continuum this transfer mapping is simply defined by the identity,

$$\mathcal{I}_{\Omega_t^s}(\psi(\boldsymbol{X}, t)) = \psi(\boldsymbol{x}(\boldsymbol{X}, t), t) = \psi(\boldsymbol{x}, t). \tag{15}$$

However, the use of different spatial interpolation strategies for the fluid and solid phases will require an appropriate transfer operator that will be described below. Specifically, for the velocity field,

$$\boldsymbol{v}(\boldsymbol{x}, t) = \mathcal{I}_{\Omega_t^s}(\boldsymbol{v}(\boldsymbol{X}, t)). \tag{16}$$

In order to complete the strong form for the solid phase, appropriate Dirichlet boundary conditions can be defined as follows,

$$\boldsymbol{x}(\boldsymbol{X}, t) = \boldsymbol{x}_0, \quad \text{on} \quad \partial\Omega_D^s. \tag{17}$$

Since the immersed solid is surrounded by the fluid, additional Neumann boundary conditions are not treated explicitly as the interaction is already accounted for in the FSI force term $\boldsymbol{\mathcal{F}}$.

2.4. Immersed solid system – weak formulation

The variational formulation of the balance of linear momentum follows the same arguments outlined in Section 2.2 and reads,

$$\langle \rho^f(\dot{\boldsymbol{v}} - \boldsymbol{g}) - \boldsymbol{\mathcal{F}}, \delta\boldsymbol{v}\rangle + \langle \boldsymbol{\sigma}^f, \nabla_{\boldsymbol{x}}(\delta\boldsymbol{v})\rangle - \langle \boldsymbol{h}, \delta\boldsymbol{v}\rangle_{\Gamma^h} = 0 \tag{18}$$

and for the conservation of mass,

$$\langle \nabla_{\boldsymbol{x}}\cdot\boldsymbol{v} - \mathcal{F}^p, \delta p\rangle = 0. \tag{19}$$

Eqs. (18) and (19) summarise the weak form for the overall problem (i.e. fluid–solid). It is convenient to split the above formulae into fluid and solid phases. Introducing the Jacobian of the deformation in the solid phase $J^s = \det(\boldsymbol{F}^s)$, taking into account the Euler–Lagrange mapping $\mathcal{I}_{\Omega_t^s}$ defined above and making use of the notation

$$\int_{\Omega_0^s} (\bullet)\cdot(\bullet)\mathrm{d}V =: \langle \bullet, \bullet\rangle_0^s \tag{20}$$

the weak form expression (18) can be rewritten as,

$$\begin{aligned}&\langle \rho^f(\dot{\boldsymbol{v}} - \boldsymbol{g}), \delta\boldsymbol{v}\rangle + \langle \boldsymbol{\sigma}^f, \nabla_{\boldsymbol{x}}(\delta\boldsymbol{v})\rangle - \langle \boldsymbol{h}, \delta\boldsymbol{v}\rangle_{\Gamma^h}\\ &\quad - \left\langle (\rho^f - \rho^s)\left(\frac{\partial}{\partial t}\mathcal{I}_{\Omega_t^s}(\boldsymbol{v}(\boldsymbol{X}, t)) - \boldsymbol{g}\right), \mathcal{I}_{\Omega_t^s}(\delta\boldsymbol{v})J^s\right\rangle_0^s\\ &\quad - \langle \boldsymbol{\sigma}^s - \boldsymbol{\sigma}^f, \nabla_{\boldsymbol{x}}\mathcal{I}_{\Omega_t^s}(\delta\boldsymbol{v})J^s\rangle_0^s = 0.\end{aligned} \tag{21}$$

[1] Contributions to the solid system are marked with $(\bullet)^s$, whereas contributions to the fluid system are marked with $(\bullet)^f$.

Similarly, the weak form expression (19) can be reformulated as,

$$\langle \nabla_{\boldsymbol{x}} \cdot \boldsymbol{v}, \delta p \rangle - \langle \dot{J}^s, \mathcal{I}_{\Omega_t^s}(\delta p) \rangle_0^s = 0. \tag{22}$$

The internal virtual work within the solid phase defined in terms of the conjugate pair $\{\boldsymbol{\sigma}^s, \nabla_{\boldsymbol{x}} \mathcal{I}_{\Omega_t^s}(\delta \boldsymbol{v})\}$ can be reformulated by means of the Piola transformation in terms of an alternative conjugate pair $\{\boldsymbol{S}^s, (\boldsymbol{F}^s)^T \nabla_{\boldsymbol{X}} \mathcal{I}_{\Omega_t^s}(\delta \boldsymbol{v})\}$ as,

$$\langle \boldsymbol{\sigma}^s, \nabla_{\boldsymbol{x}} \mathcal{I}_{\Omega_t^s}(\delta \boldsymbol{v}) J^s \rangle_0^s = \langle \boldsymbol{S}^s, (\boldsymbol{F}^s)^T \nabla_{\boldsymbol{X}} \mathcal{I}_{\Omega_t^s}(\delta \boldsymbol{v}) \rangle_0^s, \tag{23}$$

where $\boldsymbol{S}^s = 2 \frac{\partial W(\boldsymbol{C}^s)}{\partial \boldsymbol{C}^s}$ is the so-called Second Piola–Kirchhoff stress tensor and $\boldsymbol{C}^s = (\boldsymbol{F}^s)^T \boldsymbol{F}^s$ is the right Cauchy–Green tensor particularised for the solid phase. The evaluation of the fluid stress $\boldsymbol{\sigma}^f$ within the solid phase follows immediately from the definition (3) in conjunction with the incompressibility constraint as,[2]

$$\boldsymbol{\sigma}^f = -\mathcal{I}_{\Omega_t^s}(p) \boldsymbol{I} + \mu \Big(\nabla_{\boldsymbol{X}} \mathcal{I}_{\Omega_t^s}(\boldsymbol{v}) + (\nabla_{\boldsymbol{X}} \mathcal{I}_{\Omega_t^s}(\boldsymbol{v}))^T \Big) (\boldsymbol{F}^s)^{-1}. \tag{24}$$

It is worthwhile emphasising that the evaluation of the spatial gradients $\nabla_{\boldsymbol{x}} \mathcal{I}_{\Omega_t^s}(\boldsymbol{v})$ and $\nabla_{\boldsymbol{x}} \mathcal{I}_{\Omega_t^s}(\delta \boldsymbol{v})$, and the subsequent construction of the deformation gradient $\boldsymbol{F}^s$ is one of the most challenging processes in any computational immersed methodology. From the spatial discretisation point of view, various approaches have been developed, using either local elementwise shape functions such as in the Immersed Finite Element Method (IFEM) and its variants [41,36,20,35] or kernel shape functions with larger compact support such as in the Immersed Structural Potential Method (ISPM) [7,8]. This important aspect will be discussed in length in the following sections.

3. Spatial discretisation

This section introduces spatial discretisation aspects for the numerical solution of the variational weak form encompassed by expressions (21) and (22). A Finite Element based approach will be preferred to solve the underlying fluid physics in Ω using either classical Lagrangian or more advanced NURBS based shape functions. Depending on the selection of shape functions, the well-known LBB condition [5] might be violated leading to spurious numerical oscillations and possibly instability of the scheme. A well established solution to this problem relies on the modification of the test function space as defined in (6) by using stabilisation techniques based upon an alternative Petrov–Galerkin weak formulation (see [4,32,34]). In general, the domain Ω is subdivided into a finite set of non-overlapping elements $e \in \mathbb{E}$ such that,

$$\Omega^h = \bigcup_e \Omega_e, \quad \forall e \in \mathbb{E} \tag{25}$$

and all space fields included in the weak form are suitably discretised. Notice that in order to complete the semi-discrete formulation of the overall problem, the spatial discretisation of the Euler–Lagrange mapping also needs to be carried out.

3.1. Lagrangian based discretisation of the fluid

Without prejudice to the generality of the formulation, a Q2Q1 Lagrangian finite element discretisation is chosen as follows,

$$\begin{aligned} \boldsymbol{v}^h &= \sum_{A \in \omega} N^A \boldsymbol{v}_A; \quad \delta \boldsymbol{v}^h = \sum_{A \in \omega} N^A \delta \boldsymbol{v}_A, \\ p^h &= \sum_{B \in \bar{\omega}} M^B p_B; \quad \delta p^h = \sum_{B \in \bar{\omega}} M^B \delta p_B, \end{aligned} \tag{26}$$

where $N^A(\boldsymbol{x}) : \Omega^h \to \mathbb{R}$ are quadratic shape functions associated with nodes $A \in \omega = \{1, \dots, n\}$ and $M^B(\boldsymbol{x}) : \Omega^h \to \mathbb{R}$ are linear shape functions associated with nodes $B \in \bar{\omega} = \{1, \dots, m\}$. This element is known to satisfy the LBB condition and provides optimal quadratic convergence of the velocity field (see [5]). The semi-discrete balance of momentum reads,

$$\langle \rho^f (\dot{\boldsymbol{v}}^h - \boldsymbol{g}^h), \delta \boldsymbol{v}^h \rangle + \langle \boldsymbol{\sigma}^f (\boldsymbol{v}^h, p^h), \nabla_{\boldsymbol{x}} (\delta \boldsymbol{v}^h) \rangle - \langle \boldsymbol{h}^h, \delta \boldsymbol{v}^h \rangle_{\Gamma^h} = 0, \tag{27}$$

whereas the incompressibility constraint reads,

$$\langle \nabla_{\boldsymbol{x}} \cdot \boldsymbol{v}^h, \delta p^h \rangle = 0. \tag{28}$$

If necessary (i.e. for low order elements in conjunction with high Reynolds numbers), a stabilisation technique for the underlying Galerkin approach can be applied (cf. [32]) using extended test function spaces as,

$$\begin{aligned} \mathbb{V}^{\tilde{v}} &=: \{\delta \tilde{\boldsymbol{v}} \in \mathbb{H}^1(\Omega) | \delta \tilde{\boldsymbol{v}} = \delta \boldsymbol{v} + \gamma_{\text{SUPG}} \boldsymbol{v} \cdot \nabla_{\boldsymbol{x}} (\delta \boldsymbol{v}) + \gamma_{\text{PSPG}} \nabla_{\boldsymbol{x}} (\delta p)\}, \\ \mathbb{V}^{\tilde{p}} &=: \{\delta \tilde{p} \in L_2(\Omega) | \delta \tilde{p} = \delta p + \gamma_{\text{LSIC}} \nabla_{\boldsymbol{x}} \cdot (\delta \boldsymbol{v})\}, \end{aligned} \tag{29}$$

where γ_{SUPG}, γ_{PSPG} and γ_{LSIC} are precalculated stabilisation parameters (see [34] for a detailed definition of the stabilisation parameters). The modified semi-discrete balance of linear momentum reads,

$$\begin{aligned} &\langle \rho^f (\dot{\boldsymbol{v}}^h - \boldsymbol{g}^h), \delta \boldsymbol{v}^h \rangle + \langle \boldsymbol{\sigma}^f (\boldsymbol{v}^h, p^h), \nabla_{\boldsymbol{x}} (\delta \boldsymbol{v}^h) \rangle - \langle \boldsymbol{h}^h, \delta \boldsymbol{v}^h \rangle_{\Gamma^h} \\ &\quad + \sum_e \gamma_{\text{SUPG}} \langle \mathcal{R}_v, (\boldsymbol{v}^h \cdot \nabla_{\boldsymbol{x}}) \delta \boldsymbol{v}^h \rangle + \sum_e \gamma_{\text{LSIC}} \langle \mathcal{R}_p, \nabla_{\boldsymbol{x}} \cdot \delta \boldsymbol{v}^h \rangle = 0 \end{aligned} \tag{30}$$

and the kinematic constraint

$$\langle \nabla_{\boldsymbol{x}} \cdot \boldsymbol{v}^h, \delta p^h \rangle + \sum_e \gamma_{\text{PSPG}} \langle \mathcal{R}_v, \nabla_{\boldsymbol{x}} \delta \boldsymbol{p}^h \rangle = 0. \tag{31}$$

Here, $\mathcal{R}_v$ and $\mathcal{R}_p$ denote the residuals of the original momentum and kinematic constraint equations, respectively.

3.2. NURBS based discretisation of the fluid

The consideration of more sophisticated NURBS based shape functions for the spatial semi-discretisation of the problem yields,

$$\begin{aligned} \boldsymbol{v}^h &= \sum_{A \in \omega} R^A \boldsymbol{v}_A; \quad \delta \boldsymbol{v}^h = \sum_{A \in \omega} R^A \delta \boldsymbol{v}_A, \\ p^h &= \sum_{B \in \bar{\omega}} R^B p_B; \quad \delta p^h = \sum_{B \in \bar{\omega}} R^B \delta p_B, \end{aligned} \tag{32}$$

where (cf. [12,15])

$$R^{A,(i)} = R^{i,j,\hat{\imath}}_{p,q,r}(\xi) = \frac{N_{i,p}(\xi) M_{j,q}(\eta) L_{\hat{\imath},r}(\zeta) w_{i,j,\hat{\imath}}}{\sum_{\hat{i}=1}^{n} \sum_{\hat{j}=1}^{m} \sum_{\hat{\imath}=1}^{l} N_{\hat{i},p}(\xi) M_{\hat{j},q}(\eta) L_{\hat{\imath},r}(\zeta) w_{\hat{i},\hat{j},\hat{\imath}}}. \tag{33}$$

Here, p, q, r denote the order of the non-rational B-Spline shape functions N, M and L, recursively defined as follows,

$$N_{i,p} = \frac{\xi - \xi_i}{\xi_{i+p} - \xi_i} N_{i,p-i}(\xi) + \frac{\xi_{i+p+1} - \xi}{\xi_{i+p+1} - \xi_{i+1}} N_{i+1,p+1}(\xi) \tag{34}$$

starting with

$$N_{i,0}(\xi) = \begin{cases} 1 & \text{if } \xi_i \leqslant \xi < \xi_{i+1}, \\ 0 & \text{otherwise.} \end{cases} \tag{35}$$

The above system has been defined for the three dimensional case; the two dimensional case follows suit. The order of the quadratic and linear parts has to be adjusted within the recursive definition of the NURBS basis. It can be observed that the number of constraints is, in general, higher compared to Lagrangian shape functions, hence the LBB condition is violated, requiring stabilisation.

[2] Notice that the stress contribution in Ω_t^s due the fluid $\boldsymbol{\sigma}^f$ is several orders of magnitude smaller than the stress contribution due to the immersed solid $\boldsymbol{\sigma}^s$, hence it is usually neglected [41,20].

3.3. Discrete Euler–Lagrange mapping

IFEM, Lagrangian mesh. A common approach is to numerically model the immersed solid following a finite element approach (Immersed Finite Element Method (IFEM) [41]). Additional shape functions are introduced to describe the immersed solid (cf. [20]) as follows,

$$\mathcal{I}_{\Omega_t^s}(\boldsymbol{v}^h) = \sum_{C=1}^{n_{\text{node}}} \overline{N}^C \bar{\boldsymbol{v}}_C; \quad \mathcal{I}_{\Omega_t^s}(p^h) = \sum_{C=1}^{n_{\text{node}}} \overline{N}^C \bar{p}_C. \tag{36}$$

Here, $\overline{N}^C(\boldsymbol{X}) : \Omega_0^{s,h} \to \mathbb{R}$ are the corresponding shape functions and $\bar{\boldsymbol{v}}_C$ and $\bar{p}_C$ denote the nodal values at the current position of the solid, calculated from the background Eulerian fluid grid as follows,

$$\bar{\boldsymbol{v}}_C = \sum_{A\in\omega} N^A(\boldsymbol{x}(\boldsymbol{X}_C,t))\boldsymbol{v}_A; \quad \bar{p}_C = \sum_{B\in\bar{\omega}} N^B(\boldsymbol{x}(\boldsymbol{X}_C,t))p_B. \tag{37}$$

Combining formulae (36) and (37) results in the definition of the spatial interpolation operator for the transfer of information between the Eulerian and the Lagrangian meshes as follows,

$$\mathcal{I}_{\Omega_t^s}(N^A(\boldsymbol{X},t)) = \sum_{C=1}^{n_{\text{node}}} N^A(\boldsymbol{x}(\boldsymbol{X}_C,t))\overline{N}_C(\boldsymbol{X}), \tag{38}$$

which renders a linear operator. The Euler–Lagrange mapping is shown in Fig. 1 for a one dimensional system and linear shape functions. The mapping for the single immersed element reads,

$$\mathcal{I}_{\Omega_t^s}(N^A(X(\xi),t)) = N^A(x(X_1,t))\overline{N}_1(X(\xi)) + N^A(x(X_2,t))\overline{N}_2(X(\xi)). \tag{39}$$

It is crucial to realise that the finite element mesh generation of the immersed solid cannot be independent of the finite element mesh generation of the surrounding fluid phase. Indeed, a coarse solid mesh, as displayed for instance in Fig. 2, will not yield optimal results, since the background fluid shape function N^3 is not affected by the presence of the immersed solid. In other words, the numerical integration of the FSI force field $\mathcal{F}$ will not be accurately computed. From the physical point of view, this would mean that the presence of the immersed solid is not properly accounted for by the surrounding fluid, leading to unphysical breaking of the solid phase. On the other hand, an unnecessarily fine solid mesh would result in an exceedingly high condition number of the resulting tangent stiffness matrix of the system (after linearisation) leading to numerical difficulties.

IFEM, NURBS mesh. The Euler–Lagrange mapping can be redefined for the application of a NURBS based finite element fluid description in a straightforward manner. As presented previously, the Lagrangian shape functions are replaced with NURBS shape functions to calculate the nodal values,

$$\bar{\boldsymbol{v}}_C = \sum_{A\in\omega} R^A(\boldsymbol{x}(\boldsymbol{X}_C,t))\boldsymbol{v}_A; \quad \bar{p}_C = \sum_{B\in\bar{\omega}} R^B(\boldsymbol{x}(\boldsymbol{X}_C,t))p_B \tag{40}$$

leading to the interpolation-spreading operator,

$$\mathcal{I}_{\Omega_t^s}(R^A(\boldsymbol{X},t)) = \sum_{C=1}^{n_{\text{node}}} R^A(\boldsymbol{x}(\boldsymbol{X}_C,t))\overline{N}_C(\boldsymbol{X}), \tag{41}$$

which is also a linear operator.

ISPM. The last approach described in this section is the Immersed Structural Potential Method (ISPM) introduced in Gil et al. [7]. The solid is represented as a Helmholtz's free energy density functional immersed within the surrounding fluid phase. Moreover, the solid domain is modelled in a Lagrangian manner as a collection of integration points a_p immersed within the fluid, moving from an initial position $\boldsymbol{X}_{a_p}$ to the spatial position $\boldsymbol{x}_{a_p}$ through the deformation defined by the motion of the surrounding continuum (i.e. non-slip condition).

Notice that the integration points' parameters (i.e. spatial location $\boldsymbol{x}_{a_p}$ and associated tributary weight W_{a_p}) can be directly obtained on the solid domain, without the need for an initial tessellation (in the sense of a Finite Element approach). Alternatively, $\boldsymbol{X}_{a_p}$ and W_{a_p} can be obtained directly from the use of optimal high order Gaussian quadrature rules. As shown in [8], the latter approach can ensure accuracy of quadrature of the immersed potential and improve the speed of computation.

Within this approach, global shape functions $\varphi(\boldsymbol{x})$ are established on the Eulerian fluid grid to first interpolate the kinematic information directly to the solid integration points a_p and second,

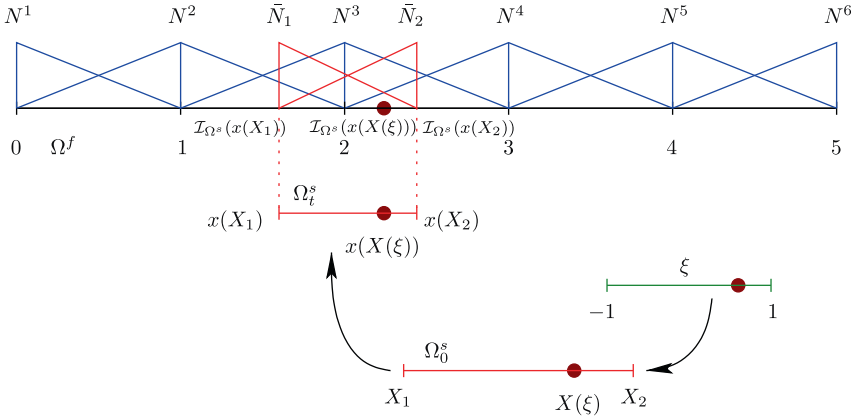

Fig. 1. One dimensional Euler–Lagrange mapping.

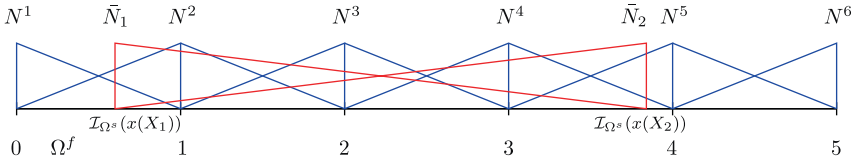

Fig. 2. Effects of a coarse solid mesh.

spread the calculated forces back to the balance of linear momentum of the fluid. The construction of the continuous functions $\varphi(\boldsymbol{x})$ starts with the approximation of the Dirac delta distribution through a tensorised discrete approximation,

$$\varphi(\boldsymbol{x}) = \prod_{i=1}^{d} \delta_{\Delta x_i}(x_i), \quad d \in [2,3], \tag{42}$$

where Δx_i is related to the size of the background fluid mesh and

$$\delta_{\Delta x_i} = \frac{1}{\Delta x_i}\phi\left(\frac{x_i}{\Delta x_i}\right) \tag{43}$$

is defined in terms of a smoothed representation ϕ of the one dimensional Dirac delta distribution, to obtain

$$\boldsymbol{v}^{a_p} = \sum_A \varphi^A(\boldsymbol{x}^{a_p})\boldsymbol{v}_A, \quad \varphi^A(\boldsymbol{x}^{a_p}) = \varphi(\boldsymbol{x}^{a_p} - \boldsymbol{x}^A) \tag{44}$$

for the interpolation of the velocity field. For details on the construction of sophisticated kernel functions, see Gil et al. [8]. More generally, we can write for the Euler–Lagrange mapping

$$\mathcal{I}_{\Omega_t^s}(\varphi^A(\boldsymbol{X},t)) = \varphi^A(\boldsymbol{x}(\boldsymbol{X},t)), \tag{45}$$

which coincides with the continuum map. A key aspect of this methodology is the direct integration of the deformable solid stresses from solid integration points to fluid nodes, similar to the Material Point Method (MPM) [40], reducing the number of interpolation operations (compare formula (45) with formulae (38) and (41)).

3.4. Calculation of the deformation gradient tensor

The evaluation of the deformation gradient tensor in the IFEM methodology at the corresponding Gauss points requires the time integration of the velocity field at each node C of the immersed solid grid to recover the actual position of the node as,

$$\bar{\boldsymbol{x}}_C \equiv \bar{\boldsymbol{x}}_C(\bar{\boldsymbol{v}}_C) = \int_{t_0}^{t} \bar{\boldsymbol{v}}(\tau)\mathrm{d}\tau. \tag{46}$$

Taking Eq. (36) into account, we can express the deformation gradient tensor in a classical Finite Element sense as,

$$\boldsymbol{F} = \sum_{C=1}^{n_{\text{node}}} \bar{\boldsymbol{x}}_C \otimes \nabla_{\boldsymbol{X}} \bar{N}^C. \tag{47}$$

For the ISPM methodology, it is necessary to integrate in time the deformation gradient tensor at any integration point a_p directly using the spatial velocity gradient tensor $\boldsymbol{l}$ defined as,

$$\boldsymbol{l} = \sum_A \boldsymbol{v}_A \otimes \nabla_{\boldsymbol{x}} \varphi^A(\boldsymbol{x}) \tag{48}$$

and the kinematic relation

$$\dot{\boldsymbol{F}} = \boldsymbol{l}\boldsymbol{F}. \tag{49}$$

For further details on an explicit representation of useful time integration schemes, refer to Gil et al. [7]. In contrast to the IFEM approach (see Eq. (47)), the evaluation of the deformation gradient tensor $\boldsymbol{F}$ in the ISPM manner (Eqs. (48) and (49)) prevents the occurrence of locking effects in the incompressibility limit. This will be shown at a later stage in this paper by means of a numerical example. Alternatively, an enhanced mode can be added into formula (47) in a Hu-Washizu multifield variational sense [1], to overcome the inherent difficulties of the IFEM approach (see Appendix A for further details).

In addition, within a full variational formulation, it is also possible to introduce the weak form of the mapping (16) as,

$$\left\langle \left(\frac{\partial \boldsymbol{x}^{\text{h}}(\boldsymbol{X},t)}{\partial t} - \mathcal{I}_{\Omega^s}(\boldsymbol{v}^{\text{h}}(\boldsymbol{X},t)) \right), \delta\boldsymbol{x}^{\text{h}} \right\rangle_0^s = 0 \tag{50}$$

if the solution and test functional spaces

$$\boldsymbol{x}^{\text{h}} = \sum_{C=1}^{n_{\text{node}}} \bar{N}^C \boldsymbol{x}_C, \quad \delta\boldsymbol{x}^{\text{h}} = \sum_{C=1}^{n_{\text{node}}} \bar{N}^C \delta\boldsymbol{x}_C \tag{51}$$

of the immersed solid are explicitly defined (cf. [20]). In contrast to the approaches described above where the number of unknowns in the system coincides with those of the fluid phase, the final system of equations is now enlarged by the number of unknowns of the immersed solid.

4. Discretisation in time

The previously introduced semi-discrete problem can now be discretised in time in order to obtain a full discrete set of non-linear algebraic equations which can be solved (i.e. via a Newton–Raphson iteration scheme). Consider a time interval $\mathbb{I} = [0,T]$ which can be split into a sequence of subintervals $n \to n+1$ of size $\Delta t = t_{n+1} - t_n$, where $(\bullet)_{n+1}$ and $(\bullet)_n$ denote values of the corresponding function at the specified time and assume that all values at time n are known.

4.1. Fluid

To approximate the state $(\boldsymbol{v}^{\text{h}}_{n+1}, p^{\text{h}}_{n+1})$ we consider a one step method for the evaluation of the weak form in (30) and (31) as follows,

$$\begin{aligned} &\left\langle \rho\left(\frac{\boldsymbol{v}^{\text{h}}_{n+1} - \boldsymbol{v}^{\text{h}}_{n}}{\Delta t} - (\boldsymbol{v}^{\text{h}}_{n+1/2}\cdot\nabla_{\boldsymbol{x}})\boldsymbol{v}^{\text{h}}_{n+1/2} - \boldsymbol{g}^{\text{h}}_{n+1/2} \right), \delta\boldsymbol{v}^{\text{h}} \right\rangle \\ &\quad + \langle \boldsymbol{\sigma}(\boldsymbol{v}^{\text{h}}_{n+1/2}, p^{\text{h}}_{n+1}), \nabla_{\boldsymbol{x}}(\delta\boldsymbol{v}^{\text{h}}) \rangle - \langle \boldsymbol{h}^{\text{h}}_{n+1/2}, \delta\boldsymbol{v}^{\text{h}} \rangle_{\Gamma^{\text{h}}} = 0, \\ &\langle \nabla_{\boldsymbol{x}}\cdot\boldsymbol{v}^{\text{h}}_{n+1}, \delta p^{\text{h}} \rangle = 0, \end{aligned} \tag{52}$$

where $(\bullet)_{n+1/2} = \frac{1}{2}((\bullet)_{n+1} + (\bullet)_n)$ denotes the mid-point configuration. Note that we evaluate the constraints at the end-point configuration and assume that the corresponding Lagrange multipliers p^{h}_{n+1} are constant within each time step. If the system requires the use of stabilisation techniques, it yields

$$\begin{aligned} &\left\langle \rho\left(\frac{\boldsymbol{v}^{\text{h}}_{n+1} - \boldsymbol{v}^{\text{h}}_{n}}{\Delta t} - (\boldsymbol{v}^{\text{h}}_{n+1/2}\cdot\nabla_{\boldsymbol{x}})\boldsymbol{v}^{\text{h}}_{n+1/2} - \boldsymbol{g}^{\text{h}}_{n+1/2} \right), \delta\boldsymbol{v}^{\text{h}} \right\rangle \\ &\quad + \langle \boldsymbol{\sigma}(\boldsymbol{v}^{\text{h}}_{n+1/2}, p^{\text{h}}_{n+1}), \nabla_{\boldsymbol{x}}(\delta\boldsymbol{v}^{\text{h}}) \rangle - \langle \boldsymbol{h}^{\text{h}}_{n+1/2}, \delta\boldsymbol{v}^{\text{h}} \rangle_{\Gamma^{\text{h}}} \\ &\quad + \sum_e \gamma_{\text{SUPG}} \langle \mathcal{R}_v(\boldsymbol{v}^{\text{h}}_{n+1/2}, p^{\text{h}}_{n+1}), (\boldsymbol{v}^{\text{h}}_{n+1/2}\cdot\nabla_{\boldsymbol{x}})\delta\boldsymbol{v}^{\text{h}} \rangle \\ &\quad + \sum_e \gamma_{\text{LSIC}} \langle \mathcal{R}_p(\boldsymbol{v}^{\text{h}}_{n+1}), \nabla_{\boldsymbol{x}}\cdot\delta\boldsymbol{v}^{\text{h}} \rangle = 0, \\ &\langle \nabla_{\boldsymbol{x}}\cdot\boldsymbol{v}^{\text{h}}_{n+1/2}, \delta p^{\text{h}} \rangle \\ &\quad + \sum_e \gamma_{\text{PSPG}} \langle \mathcal{R}_v(\boldsymbol{v}^{\text{h}}_{n+1/2}, p^{\text{h}}_{n+1}), \nabla_{\boldsymbol{x}}\delta\boldsymbol{p}^{\text{h}} \rangle = 0. \end{aligned} \tag{53}$$

This mid-point type rule (see [3]) is of second order accuracy and robust for large time step sizes, as will be demonstrated numerically in a later section of this paper.

4.2. Immersed solid

The additional immersed solid contributions defined in (21) and (22) for the solid domain need also to be discretised in time. The contribution to the linear momentum balance equation gives,

$$\begin{aligned} &\mathcal{F}^{\text{h}}(\boldsymbol{v}_n, \boldsymbol{v}_{n+1}, p_{n+1}) \\ &\quad = -\left\langle (\rho_0^f - \rho_0^s)\left(\frac{\mathcal{I}_{\Omega^s}(\boldsymbol{v}^{\text{h}}_{n+1}) - \mathcal{I}_{\Omega^s_t}(\boldsymbol{v}^{\text{h}}_{n})}{\Delta t} - \boldsymbol{g}^{\text{h}}_{n+1/2} \right), \mathcal{I}_{\Omega^s_t}(\delta\tilde{\boldsymbol{v}}^{\text{h}}) \right\rangle_0^s \\ &\qquad - \langle \tilde{\boldsymbol{S}}^s, (\boldsymbol{F}^s(\mathcal{I}_{\Omega^s_t}(\boldsymbol{v}^{\text{h}}_{n+1/2})))^T \nabla_{\boldsymbol{X}} \mathcal{I}_{\Omega^s_t}(\delta\tilde{\boldsymbol{v}}^{\text{h}}) \rangle_0^s \\ &\qquad + \langle \bar{\boldsymbol{\sigma}}^f(\mathcal{I}_{\Omega^s_t}(\boldsymbol{v}^{\text{h}}_{n+1/2}), \mathcal{I}_{\Omega^s_t}(p^{\text{h}}_{n+1})), \nabla_{\boldsymbol{x}} \mathcal{I}_{\Omega^s_t}(\delta\tilde{\boldsymbol{v}}^{\text{h}}) J^s(\mathcal{I}_{\Omega^s_t}(\boldsymbol{v}^{\text{h}}_{n+1/2})) \rangle_0^s \end{aligned} \tag{54}$$

and the additional contribution to the kinematic constraint becomes,

$$\mathcal{F}^{p,\mathrm{h}}(\boldsymbol{v}_n,\boldsymbol{v}_{n+1}) = -\left\langle \left(\frac{J^s(\mathcal{I}_{\Omega_t^s}(\boldsymbol{v}^{\mathrm{h}}_{n+1})) - J^s(\mathcal{I}_{\Omega_t^s}(\boldsymbol{v}^{\mathrm{h}}_{n}))}{\Delta t} \right), \mathcal{I}_{\Omega_t^s}(\delta\tilde{p}^{\mathrm{h}}) \right\rangle_0^s . \tag{55}$$

The evaluation of the second Piola–Kirchhoff stress tensor $\tilde{\boldsymbol{S}}^s$ in (54) is inspired by the development of energy–momentum schemes for solid mechanics,

$$\tilde{\boldsymbol{S}}^s = 2DW(\boldsymbol{C}_{n+1/2}) + 2\frac{W(\boldsymbol{C}_{n+1}) - W(\boldsymbol{C}_n) - \boldsymbol{S}^s(\boldsymbol{C}_{n+1/2}) : (\boldsymbol{C}_{n+1} - \boldsymbol{C}_n)}{\|\boldsymbol{C}_{n+1} - \boldsymbol{C}_n\|^2}(\boldsymbol{C}_{n+1} - \boldsymbol{C}_n), \tag{56}$$

which provide enhanced stability for large time steps (see [2]). Specifically, for a St. Venant–Kirchhoff material the discrete gradient in (56) is equal to the evaluation of the strain energy function at the mid-point of the strains, i.e. $\tilde{\boldsymbol{S}}^s = 2DW(\boldsymbol{C}_{n+1/2})$. Furthermore, this approach also shows enhanced stability for Neo-Hookean materials as presented in [10]. These two constitutive models will be employed in the numerical examples presented at a later stage in this paper.

4.3. Euler–Lagrange mapping

The Euler–Lagrange mapping requires an algorithmic search process to identify the local coordinates for the evaluation of the shape functions (i.e. $N^A(\boldsymbol{x}(\boldsymbol{X}_C,t))$. A similar process is also needed in contact mechanics on the actual contact surface and hence, can be applied with very few modifications to the problem at hand. In particular, a local Newton–Raphson iteration process is used to calculate the local values of N^A for each node $\boldsymbol{x}_C$. We cannot incorporate this iterative scheme within the mid-point type discretisation without cumbersome modifications. An approach proposed in Hesch and Betsch [11] for contact problems would increase unnecessarily the total number of unknowns, limiting the efficiency of the overall algorithm. Thus, we resort to evaluating the mapping (38) itself at time n as follows,

$$\mathcal{I}_{\Omega_t^s}(N^A(\boldsymbol{X},t)) = \sum_{C=1}^{n_{\mathrm{node}}} N^A(\boldsymbol{x}(\boldsymbol{X}_C,t_n))\overline{N}_C(\boldsymbol{X}). \tag{57}$$

This approach has also been proposed in Hesch and Betsch [11] where it has been shown to be very suitable for contact problems. A similar approach is followed in the case of the IFEM-NURBS mapping (41) or the ISPM mapping (45).

5. Numerical examples

In this section, we aim to evaluate in a comprehensive manner the different continuum immersed approaches presented above. In particular, we compare the convergence and numerical performance of the IFEM and the ISPM. The whole computational algorithm has been programmed in MATLAB using C++ MEX implementations for the core functionality. A standard iterative GMRES solver is used to solve the linear system arising as a result of each Newton–Raphson iteration.

5.1. Free falling cylinder

We consider a well established benchmark problem whose analytical solution is known. The problem is defined by a free falling cylinder immersed in a viscous Newtonian incompressible fluid of viscosity $\mu^f = 0.1$, modelled within a two-dimensional setup. The geometry of the problem as well as the boundary conditions are shown in Fig. 3. Both the solid and the fluid are subjected to a gravitational force field with acceleration defined by $g = 9.81$. The density of the fluid is taken as $\rho^f = 1000$ whereas the density of the solid is $\rho^s = 1200$. For a rigid cylinder, the analytical solution for the terminal velocity v^{end} reads,

$$v^{end} = \frac{(\rho^s - \rho^f)ga^2}{4\mu^f}\left[\ln\left(\frac{L}{a}\right) - 0.9157 + 1.7244\left(\frac{a}{L}\right)^2 - 1.7302\left(\frac{a}{L}\right)^4\right], \tag{58}$$

where the following parameters $L = 0.02$ and $a = 0.0025$ have been used for this specific simulation. Isoparametric quadrilateral finite elements will be used to model numerically the fluid and the immersed solid, the latter being always linear. For the IFEM methodology, the immersed solid is approximated by means of a Neo-Hookean constitutive law defined by,

$$W(\boldsymbol{C}) = \frac{\mu^s}{2}[\mathrm{tr}(\boldsymbol{C}) - 2] + \frac{\lambda^s}{2}(\ln J)^2 - \mu^s \ln J, \tag{59}$$

where the Lamé parameters are taken as $\lambda^s = 1537.845857$ and $\mu^s = 384.461538$ which corresponds to a Young's modulus E of 1076 and a Poisson ratio ν of 0.4. For the ISPM approach, a simplified incompressible Neo-Hookean law defined by,

$$W(\boldsymbol{C}) = \frac{\mu^s}{2}[\mathrm{tr}(\hat{\boldsymbol{C}}) - 2]; \quad \hat{\boldsymbol{C}} = J^{-2/3}\boldsymbol{F}^T\boldsymbol{F} \tag{60}$$

is evaluated at each integration point a_p. In this case, the nodes of the solid finite element mesh are not required for computational purposes.

Firstly, the results for the IFEM approach are shown in Figs. 4 and 5. Fig. 4 displays the convergence results for a Q1Q1 fluid finite element discretisation whereas Fig. 5 displays the convergence results for a Q2Q1 Taylor–Hood finite element discretisation [5]. The terminal velocity reached by both approaches converges to the same value, slightly overestimating the analytical result for the rigid case.

As can be observed, all the numerical simulations have been run with the same solid finite element mesh comprised of 1600 elements, except for the finest fluid simulation of 384×288 Q2Q1 elements, where a finer solid mesh of 3774 elements has been utilised in order to ensure the accurate description of the solid phase (i.e. the accurate spatial integration of the immersed solid stored energy functional, cf. Fig. 2).

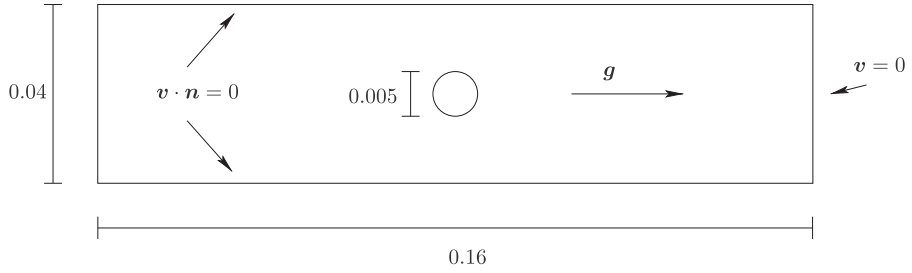

Fig. 3. Geometry and boundary conditions for the free falling cylinder.

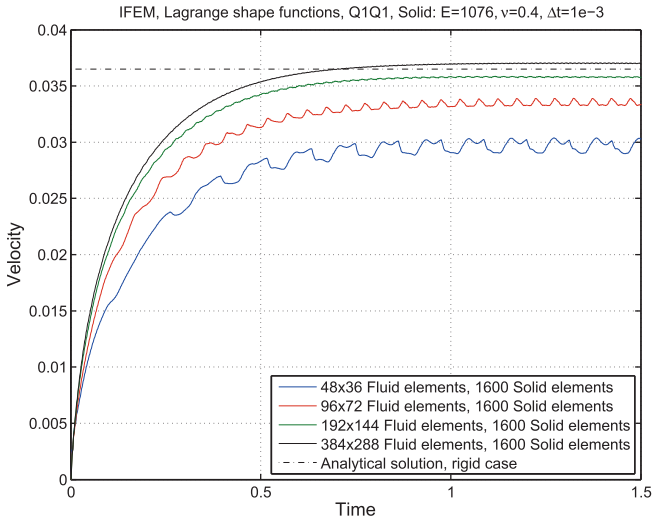

Fig. 4. IFEM, Q1Q1 fluid element.

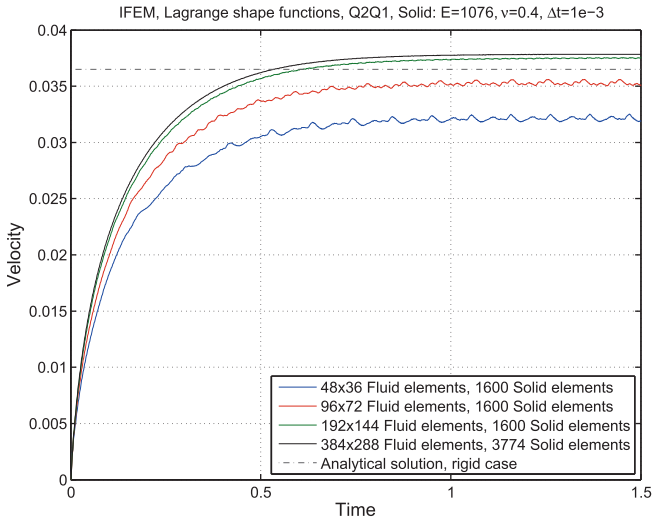

Fig. 5. IFEM, Q2Q1 fluid element.

Remark: A mesh of 384×288 Q2Q1 elements consists of 998,691 unknowns including 111,265 Lagrange multipliers for the pressure field. In contrast, a mesh of 384×288 Q1Q1 elements consists of 333,795 unknowns and the same number of Lagrange multipliers as used for the Q2Q1 formulation. The number of nodes used to set up a mesh of 384×288 Q1Q1 elements (111,265) is identical to the number of nodes used for a mesh of 192×144 Q2Q1 elements. Furthermore, a mesh of 384×288 quadratic NURBS based Q2Q1 elements consists of 333,122 unknowns including 110,592 Lagrange multipliers. Thus, the mesh of 384×288 quadratic NURBS elements is comparable (in terms of unknowns) to meshes of 384×288 Q1Q1 and 192×144 Q2Q1 Lagrangian elements.

Notice the existence of numerical oscillations in the diagrams, which are clearly related to the fluid mesh discretisation, decreasing as the fluid mesh is refined. These oscillations emanate from the lack of C^1 regularity of the shape functions across fluid finite element interfaces, typical of a Finite Element methodology. This lack of regularity introduces artificial jumps in the fluid stress field which generate artificial oscillations in the resulting velocity field. Furthermore, these artificial fluid oscillations are propagated into the immersed solid phase through the Euler–Lagrange mapping operator, activating high deformation eigenmodes within the solid (i.e. oscillations of higher frequency). All in all, two families of oscillations, emanating from the fluid and solid phases, coexist and can be observed in the above diagrams.

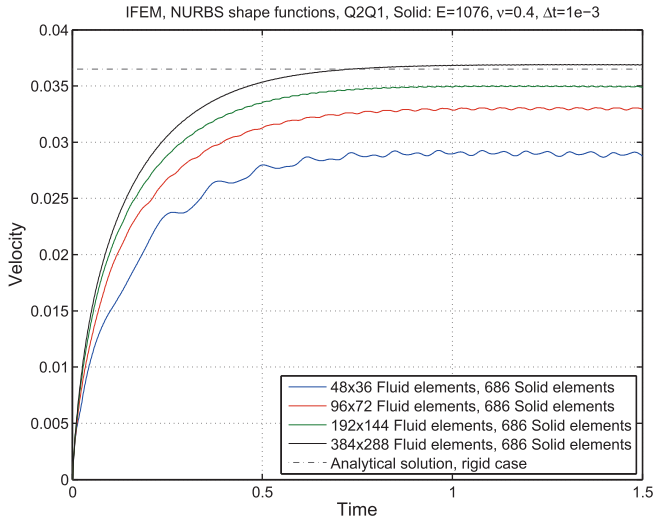

Fig. 6. IFEM, Q2Q1 NURBS fluid element.

The diagram in Fig. 6 displays the results for the Q2Q1 NURBS finite element discretisation. Notice that the Q1Q1 NURBS based discretisation matches exactly the Lagrangian based discretisation, hence it has not been analysed. Results compare well with those obtained by using Lagrangian shape functions, where the numerical oscillations, despite being also present, are slightly damped down due to the smoother nature of the NURBS fluid spatial discretisation. As previously remarked, the example using 384×288 Q2Q1 NURBS elements consists of a similar number of unknowns as the example in Fig. 4 using 384×288 Q1Q1 Lagrangian elements. In general, the use of higher order NURBS shape functions produces smoother results when compared with Lagrangian shape functions, see Cottrell et al. [17] and Bazilevs et al. [39].

Fig. 7 displays the results for a given fixed spatial discretisation (using the IFEM and a Q2Q1 Lagrangian based shape function) with various time step sizes Δt. This diagram aims to analyse the effect of the time integration scheme within the overall computational algorithm. As can be noticed, the terminal velocity is independent of the time step used within a suitable range, chosen based upon accuracy and stability. This clearly demonstrates the robustness of the implicit time integration scheme. Moreover, it can be deduced that the numerical oscillations observed in previous figures cannot be attributed to the time integrator, but to the spatial semi-discretisation approach.

The diagrams in Figs. 8 and 9 display the results for the alternative ISPM method, considering Q1Q1 and Q2Q1 Lagrangian based fluid element discretisations and a spline-based kernel function for the interpolation operator (see Eqs. (42) and (43)). Specifically, the following one-dimensional spline-based kernel function was employed [8]

$$\phi(r) = \begin{cases} 0, & r \leqslant -2, \\ \frac{r}{4} + \frac{5}{8} - \frac{\sqrt{-4r^2-12r-7}}{8}, & r \leqslant -1, \\ \frac{3}{8} + \frac{r}{4} + \frac{\sqrt{-4r^2-4r+1}}{8}, & r \leqslant 0, \\ -\frac{r}{4} + \frac{3}{8} + \frac{\sqrt{-4r^2+4r+1}}{8}, & r \leqslant 1, \\ \frac{5}{8} - \frac{r}{4} - \frac{\sqrt{-4r^2+12r-7}}{8}, & r \leqslant 2, \\ 0, & r > 2. \end{cases} \tag{61}$$

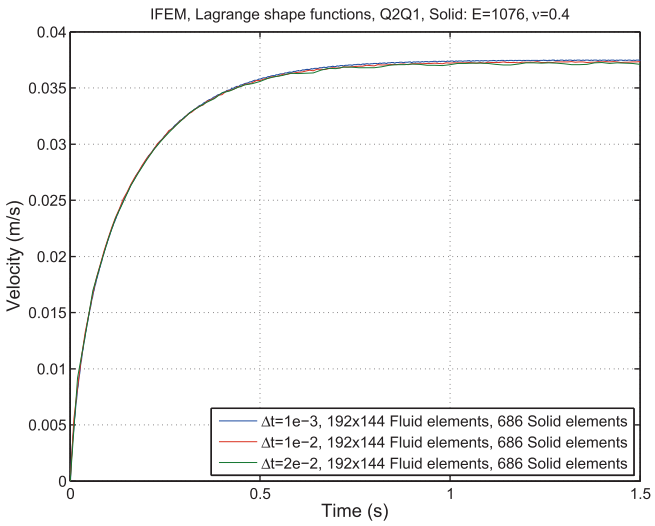

Fig. 7. Comparison of different time steps sizes.

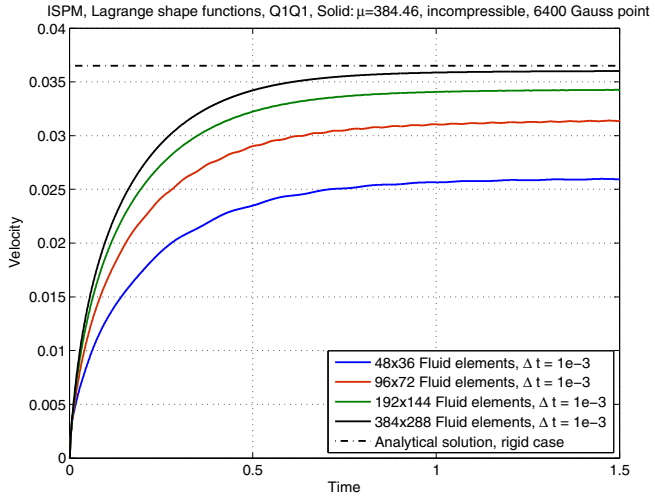

Fig. 8. ISPM, Q1Q1 fluid element.

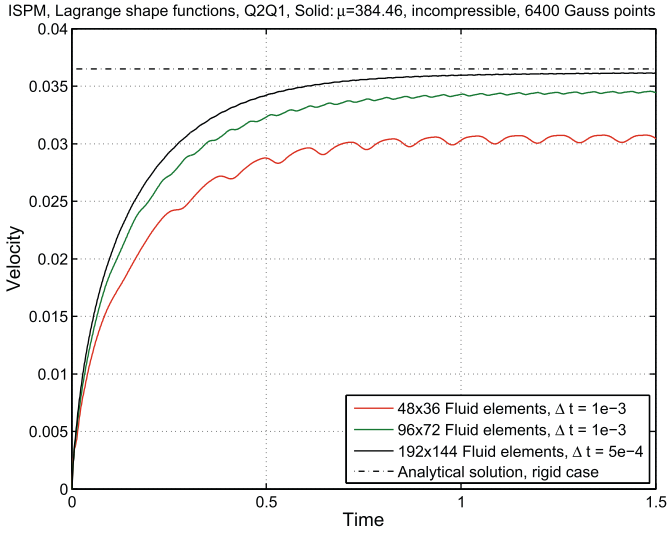

Fig. 9. ISPM, Q2Q1 fluid element.

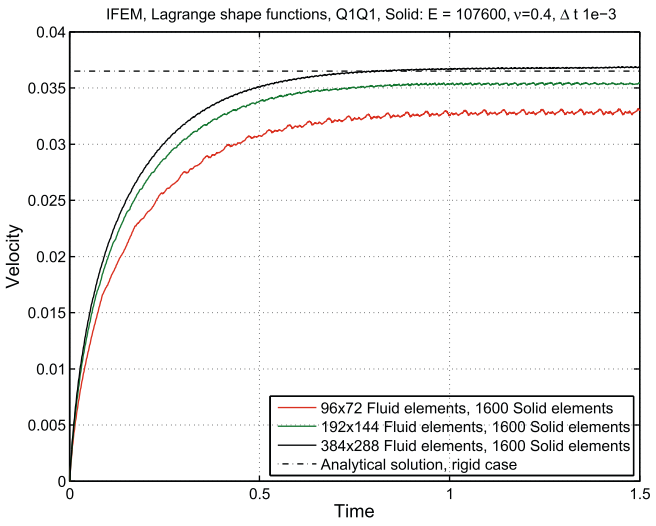

Fig. 10. IFEM, Q1Q1 fluid element.

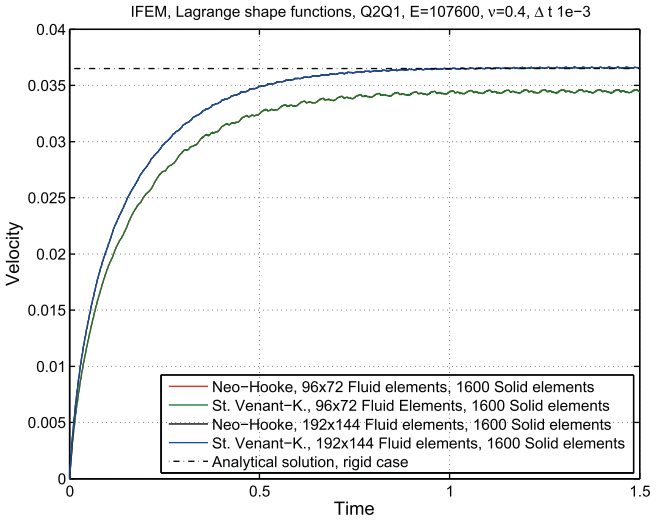

Fig. 11. IFEM, Q2Q1 fluid element.

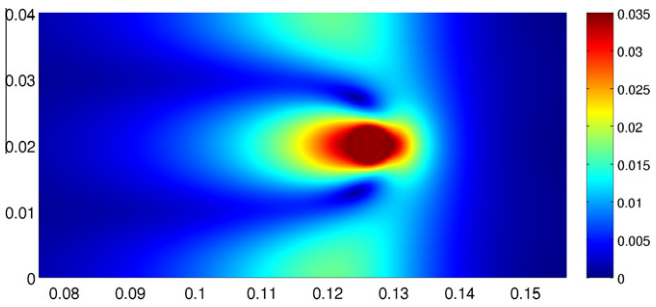

Fig. 12. Velocity field at time $t = 1.5$.

The integration points a_p used for the integration of the immersed solid energy functional are taken as the Gauss points of the underlying finite element discretisation. In this case, the terminal velocity is underestimated, in contrast to the IFEM approach where it was overestimated (see Figs. 4–6). The results for the Q1Q1 fluid element discretisation are in perfect correlation with the results

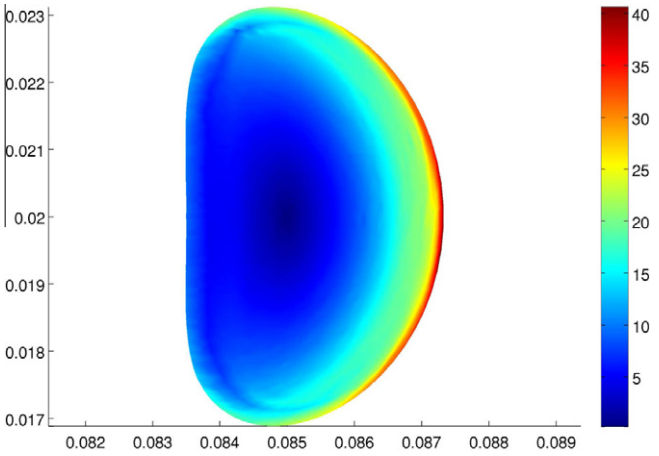

Fig. 13. Deformation after $t = 0.085$ seconds and von Mises stresses.

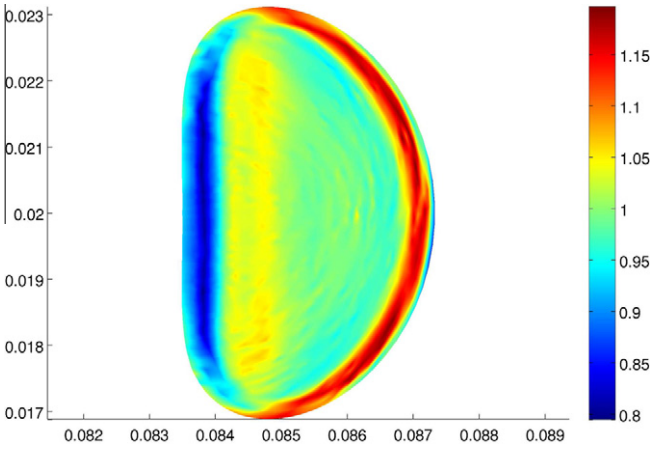

Fig. 14. Determinant of the deformation gradient tensor.

presented in Gil et al. [7] where convergence of the ISPM is demonstrated for a 768×576 Cartesian Finite Volume staggered fluid mesh.

The smoother nature of the spline-based kernel functions [8] used in the Euler–Lagrange mapping damps down considerably the artificial oscillations with respect to the IFEM approach. Crucially, in Fig. 8 the oscillations are nearly removed, making it a very competitive approach. The absolute error in the terminal velocity for coarse meshes seems to be larger than that of the IFEM. However, the artificial oscillations shown in Figs. 4 and 5 have a significant influence on the global behaviour of the overall system, which cannot be disregarded. These kernel functions fulfil $\mathcal{C}^1$ regularity across fluid element interfaces and have a fast decaying Fourier transform, which translates to quicker dampening of spurious high frequency modes present in the solution. An extensive analysis of the smoothing properties of these spline-based kernels can be found in Ref. [8].

Figs. 10 and 11 display the results of the problem using a Young's modulus two-order of magnitude higher, that is $E = 107{,}600$. As expected, both fluid discretisations, Q1Q1 and Q2Q1, converge now to the correct value of terminal velocity $v^{end} = 0.0365$. With the purpose of comparing the effect of an alternative constitutive model, we have included the results for a Saint Venant–Kirchhoff constitutive law for the Q2Q1 element in Fig. 11. As expected, since the problem at hand deals with small deformations, the behaviour of the material remains quasi-linear and the convergence curves coincide for different constitutive laws.

Let us emphasise that a 192×144 fluid mesh results in 250515 degrees of freedom for the Q2Q1 finite element discretisation and in 83955 degrees of freedom for the Q1Q1 discretisation. Naturally, it can clearly be observed that the convergence is directly linked to the number of degrees of freedom employed in the numerical simulation. As shown in Figs. 10 and 11 compared to Figs. 4, 5, 6, 8, 9, the material properties of the immersed solid dominates the global error behaviour (i.e. accurate characterisation of the rigid cylinder). As mentioned above, a compatible discretisation is required for both phases to guarantee the accurate representation of the FSI effect and prevent the ill-conditioning of the tangent stiffness matrix for the Newton–Raphson iterative scheme. The diagram in Fig. 12 shows the norm of the velocity field at time $t = 1.5$ for the ISPM approach using 192×144 Q1Q1 fluid elements, in agreement with [7].

Finally, it is worthwhile to note that for the example included in this section, the immersed body shows a quasi incompressible behaviour ($\max(\dot{J}) \approx 10^{-8}$), so neither the compressible part of the Neo-Hookean formulation nor the modification of the kinematic constraint in (22) have any significant effect on the final result. In the following section, a compressible immersed system will be analysed to demonstrate the effect of these modifications in the constitutive law and the conservation of mass equation.

Highly deformable cylinder. To demonstrate the suitability of the described approach for an immersed compressible solid, we set the Lamé parameters to $\lambda^s = 0$ and $\mu^s = 5.36$ corresponding to a Young's modulus of $E = 10.76$ and a Poisson ratio of $\nu = 0$. This way, the effects of a highly deformable and compressible cylinder can be studied. In this case, 192×144 Q2Q1 Taylor–Hood fluid and 1600 solid elements are used for the calculation and the IFEM approach is used. The deformation after $t = 0.085$ and the von Mises stresses are shown in Fig. 13. As expected, the highest stresses can be observed near the leading edge of the immersed cylinder. Fig. 14 shows the distribution of the determinant of the deformation ten-

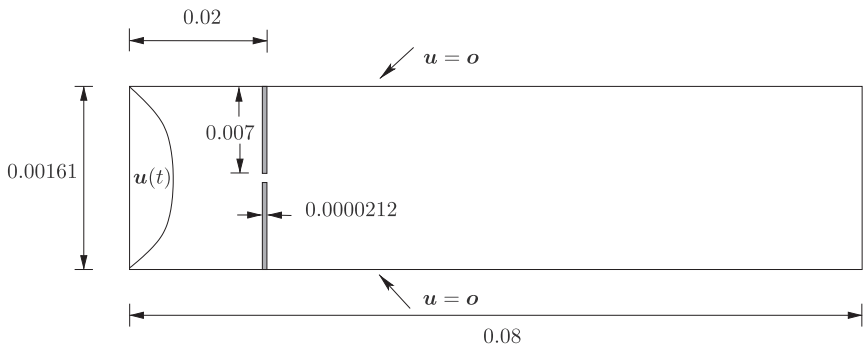

Fig. 15. Geometry and boundary conditions for an idealised bi-leaflet valve.

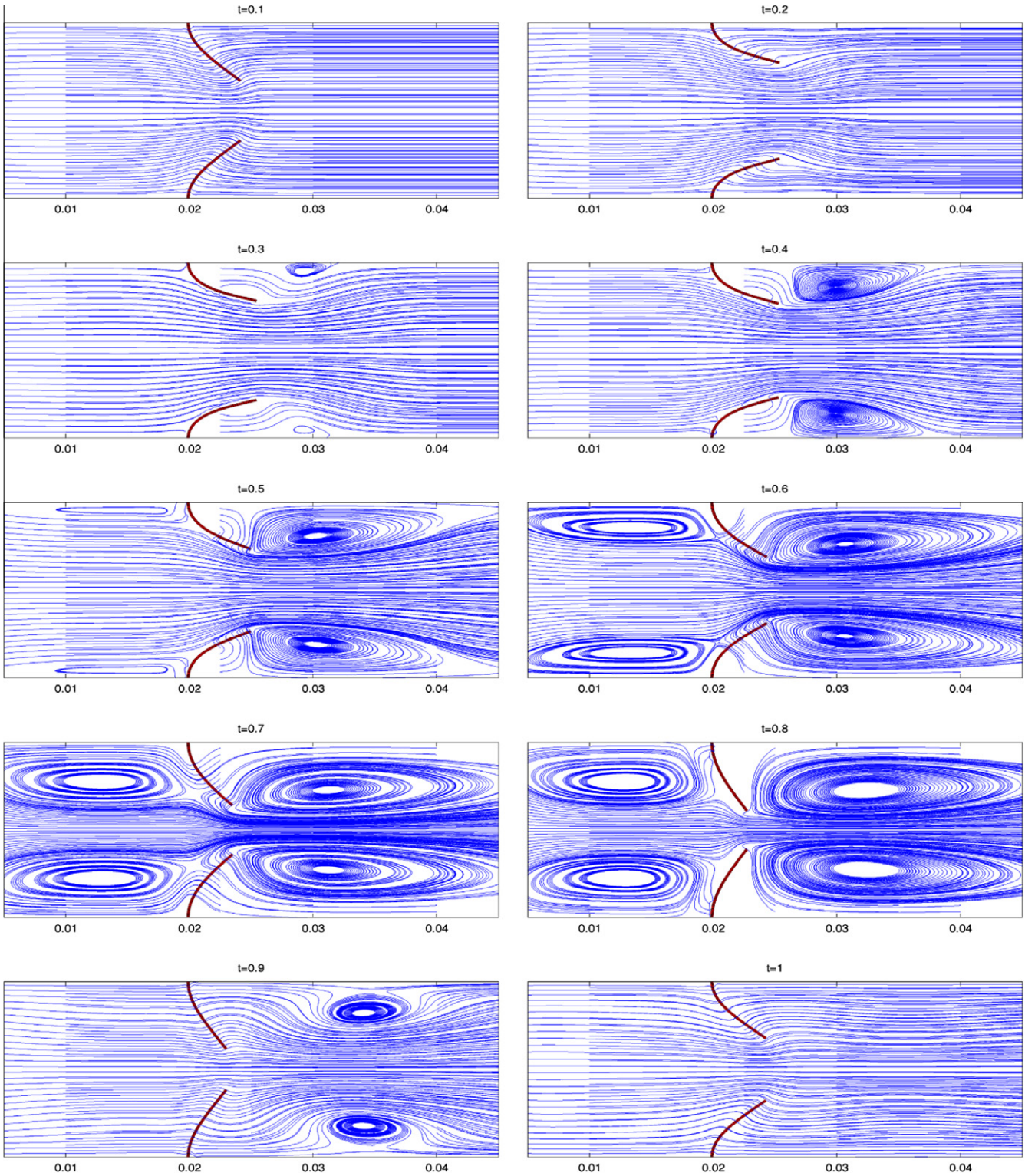

Fig. 16. Time evolution of the leaflets and streamlines of the fluid.

sor $\det(\boldsymbol{F})$ which illustrates the different areas of compression and expansion within the immersed solid.

5.2. Idealised bi-leaflet valve

The next example is extracted from [7] and is explored in order to study the suitability of an immersed continuum methodology to the analysis of FSI haemodynamical problems. An idealised two-dimensional channel is considered filled with an incompressible Newtonian viscous fluid with viscosity $\mu = 1$ and density $\rho = 1 \cdot 10^5$ mimicking the behaviour of the blood. Two leaflets are inserted into the channel, as seen in Fig. 15, representing the behaviour of an idealised two-leaflet valve. The top and bottom boundaries of the channel are fixed (i.e. homogeneous Dirichlet boundary conditions), a pulsatile non-reversible inflow is applied at the left hand boundary using the time-varying amplitude func-

tion $A(t) = 5 \cdot (\sin(2\pi t) + 1.1)$ and homogeneous Neumann boundary conditions are imposed at the right hand boundary. The leaflets are modelled as Neo-Hookean immersed solids using the Lamé parameters $\lambda^s = 8 \cdot 10^6$ and $\mu^s = 2 \cdot 10^6$ corresponding to a Young's modulus of $E = 5.6 \cdot 10^6$ and a Poisson ratio of $\nu = 0.4$. The leaflets are deliberately shortened to leave a gap between them, in order to simulate the behaviour of a regurgitating mitral valve due to stiffened (stenotic) leaflets (cf. Gil et al. [7]). For the numerical results presented in this section, the IFEM approach will be selected and compared against the results obtained in [7] by using the ISPM approach.

The series of diagrams in Fig. 16 show the time evolution for the pulsatile flow and deformation of the membranes using a 256×64 Q1Q1 fluid mesh discretisation and 40×4 linear solid elements. The obtained deformation patterns are as expected and in correlation with those reported in [7] with the alternative ISPM methodology. The results demonstrate that the IFEM immersed continuum approach is able to successfully model the inclusion of highly deformable structures into the fluid without the need for expensive moving/remeshing algorithms. The methodology allows for very simple and robust treatment of the structure.

This example has been analysed for a series of fluid discretisations in order to study the convergence pattern of the algorithm. The movement of the tip of the upper leaflet in the ox and oy directions are shown in Figs. 17 and 18, respectively, for different discretisations. The results based on the Q1Q1 fluid finite element discretisation converge to the results of the Q2Q1 fluid finite element discretisation for a sufficiently fine mesh. Once again, converged results are in perfect agreement with those obtained with the ISPM shown in Gil et al. [7].

5.3. Idealised bi-leaflet valve – locking effects

In this subsection, the example described in the previous subsection is analysed again for different solid material parameters. The objective is to investigate possible locking effects in the case of a nearly incompressible behaviour, using a Young's modulus of $E = 5.6 \cdot 10^7$ and a Poisson ratio of $\nu = 0.4990$ for both leaflets. The simulation is carried out by using the IFEM approach and the fluid is discretised using 128×32 Q2Q1 Taylor–Hood elements.

The lower membrane is modelled with a standard displacement-based isoparametric quadrilateral linear finite element. It is expected that for this discretisation, the membrane should experience locking effects, classical in displacement-based formulations (see Eq. (47)). On the other hand, the upper membrane is modelled by means of an enhanced finite element model, whose detailed formulation is presented in Appendix A). In this case, it is expected that the enhanced model should overcome any locking difficulties.

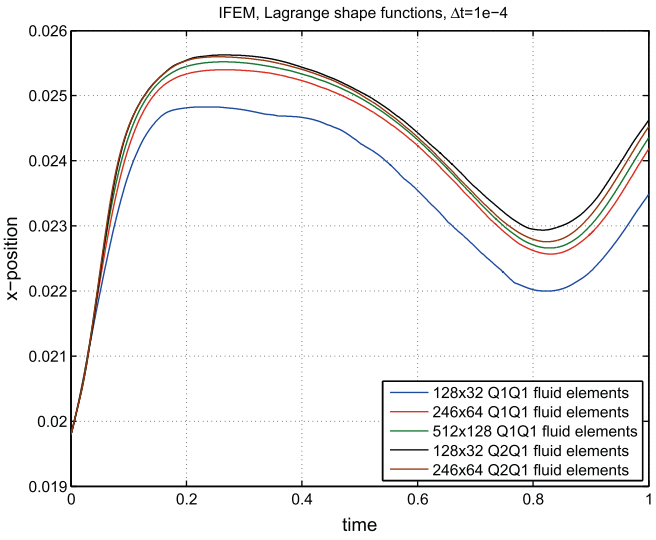

Fig. 17. X-position of the tip of the upper leaflet.

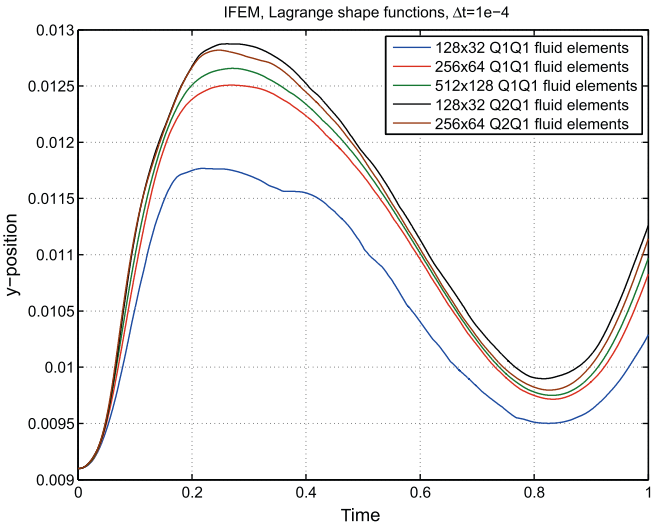

Fig. 18. Y-position of the tip of the upper leaflet.

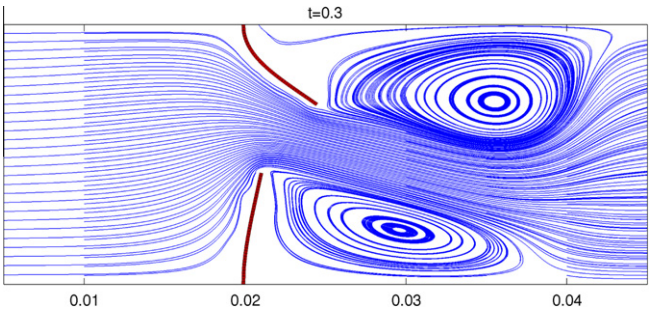

Fig. 19. Idealised bi-leaflet valve. Locking effects.

Fig. 19 displays the streamlines after $t = 0.3$ and the resulting deformation of the leaflets. Despite the fact that the streamlines should show a symmetrical pattern with respect to the *ox* axis for this Reynolds number regime, a clear locking effect can be observed in the lower leaflet. On the other hand, the upper leaflet deforms as expected, demonstrating the need to implement enhanced solid finite elements in the range of nearly incompressible scenarios for the IFEM approach. When using the ISPM approach, these locking effects are not observed [7,8]. This stems from the fact that the deformation gradient tensor $\boldsymbol{F}$ is obtained after time integration of the spatial velocity gradient tensor $\boldsymbol{l}$, which is evaluated from the Euler–Lagrange mapping (see Eqs. (48) and (49)).

6. Conclusions

In this paper, the Immersed Finite Element Method (IFEM), introduced in [41] for the analysis of solid systems immersed within an incompressible Newtonian viscous fluid, is further enhanced by means of three new updates. Firstly, a key improvement is the modification of the conservation of mass equation in the background fluid (i.e. divergence free velocity field) in order to include the possibility of non-isochoric deformations within the solid

phase. Secondly, in the incompressible limit for the solid phase, an enhanced evaluation of the deformation gradient tensor is introduced in a multifield Hu-Washizu sense to overcome locking effects. The methodology has been thoroughly analysed and compared against the alternative Immersed Structural Potential Method (ISPM), recently formulated in [7].

Thirdly, an implicit one-step time integration scheme, with enhanced stability properties, has been implemented in conjunction with consistent Newton–Raphson linearisation for optimal quadratic convergence. The resulting monolithic methodology has been comprehensively assessed for a range of Lagrangian and NURBS based shape functions for a series of numerical examples, in order to study the effect of the spatial semi-discretisation in the solution. Numerical oscillations have been observed due to the lack of C^1 regularity across element interfaces. As expected, the refinement of the fluid mesh minimises the appearance of the oscillations. Furthermore, the highest regularity of the kernel functions used for the Euler–Lagrange mapping in the ISPM approach provides excellent results, even for extreme coarse meshes with low order fluid discretisation.

Acknowledgements

This work was partially supported by the UK Engineering and Physical Sciences Research Council (EPSRC) through the Grant EP/F03010X, whose support is gratefully acknowledged.

Appendix A. Enhanced finite elements

Immersed solids modelled by means of the IFEM approach are subject to volumetric locking effects in the incompressible limit, analogous to those experienced by standard solids when using displacement-based elements. To prevent the occurrence of those effects, the deformation gradient tensor is enhanced as follows

$$\boldsymbol{F}^{\mathrm{h}} = \sum_{C=1}^{n_{\mathrm{node}}} \tilde{\boldsymbol{x}}_C \otimes \widehat{\mathrm{Grad}}_X(\overline{N}^C) + \sum_{C=1}^{n_{\mathrm{enh}}} \boldsymbol{\alpha}_C \otimes \widetilde{\mathrm{Grad}}_X(\overline{M}^C), \tag{62}$$

where

$$\widehat{\mathrm{Grad}}(\overline{N}^C) = \mathrm{Grad}_0(\overline{N}^C) + \sum_{J=1}^{4} \gamma_J^C \widetilde{\mathrm{Grad}}_X(\mathcal{H}^J). \tag{63}$$

Here, $\boldsymbol{\gamma}_J$ are gamma-stabilization vectors, $\mathcal{H}^J$ hourglass functions and

$$\widetilde{\mathrm{Grad}}_X(\bullet) = \frac{j_0}{j(\boldsymbol{\xi})} \boldsymbol{J}_0^{-T} \mathrm{Grad}_\xi(\bullet). \tag{64}$$

For further details regarding this implementation, see Belytschko et al. [1]. The consideration of a three field Hu-Washizu functional yields

$$\delta\boldsymbol{\alpha} \cdot \left[\int_{B_0} \widetilde{\mathrm{Grad}}_X(M^A) \cdot \boldsymbol{S}^s_{n,n+1} \boldsymbol{F}^{\mathrm{h}}_{n+\frac{1}{2}} \mathrm{d}V \right] = \boldsymbol{0} \tag{65}$$

to solve for the discrete unknowns $\boldsymbol{\alpha}^h = \sum_{C=1}^{n_{\mathrm{enh}}} M^C \boldsymbol{\alpha}_C$ (cf. [10]). Since the additional unknowns are local within each element we can condense the system and recover $\boldsymbol{\alpha}_{C,n+1}$ afterwards.

References

[1] T. Belytschko, J.S. Ong, W.K. Liu, J.M. Kennedy, Hourglass control in linear and nonlinear problems, Comput. Methods Appl. Mech. Engrg. 43 (1984) 251–276.
[2] P. Betsch, P. Steinmann, Conserving properties of a time FE method. Part II: Time-stepping schemes for non-linear elastodynamics, Int. J. Numer. Methods Engrg. 50 (2001) 1931–1955.
[3] P. Betsch, P. Steinmann, Conservation properties of a Time FE Method. Part III: Mechanical systems with holonomic constraints, Int. J. Numer. Methods Engrg. 53 (2002) 2271–2304.
[4] A.N. Brooks, T.J.R. Hughes, Streamline upwind/Petrov–Galerkin formulations for convection dominated flows with particular emphasis on the incompressible Navier–Stokes equations, Comput. Methods Appl. Mech. Engrg. 32 (1982) 199–259.
[5] J. Donea, A. Huerta, Finite Element Methods for Flow Problems, John Wiley & Sons, 2003.
[6] A. Gerstenberger, W.A. Wall, An eXtended finite element method/Lagrange multiplier based approach for fluid–structure interaction, Comput. Methods Appl. Mech. Engrg. 198 (2008) 1699–1714.
[7] A.J. Gil, A. Arranz Carreño, J. Bonet, O. Hassan, The immersed structural potential method for haemodynamic applications, J. Comput. Phys. 229 (2010) 8613–8641.
[8] A.J. Gil, A. Arranz Carreño, J. Bonet, O. Hassan, An enhanced Immersed Structural Potential Method for fluid–structure interaction, J. Comput. Phys., submitted for publication.
[9] H. Gómez, T.J.R. Hughes, X. Nogueira, V.M. Calo, Isogeometric analysis of the isothermal Navier–Stokes–Korteweg equations, Comput. Methods Appl. Mech. Engrg. 199 (2010) 1828–1840.
[10] C. Hesch, P. Betsch, Energy–momentum consistent algorithms for dynamic thermomechanical problems – application to mortar domain decomposition problems, Int. J. Numer. Methods Engrg. 86 (2011) 1277–1302.
[11] C. Hesch, P. Betsch, Transient 3d contact problems – Mortar method: mixed methods and conserving integration, Comput. Mech. 48 (2011) 461–475.
[12] C. Hesch, P. Betsch, Isogeometric analysis and domain decomposition methods, Comput. Methods Appl. Mech. Engrg. 213 (2012) 104–112.
[13] G.A. Holzapfel, Nonlinear Solid Mechanics, John Wiley & Sons, 2001.
[14] T.J.R. Hughes, The Finite Element Method, Dover Publications, 2000.
[15] T.J.R. Hughes, J.A. Cottrell, Y. Bazilevs, Isogeometric analysis: CAD, finite elements, NURBS, exact geometry and mesh refinement, Comput. Methods Appl. Mech. Engrg. 194 (2005) 4135–4195.
[16] I. Akkerman, Y. Bazilevs, V.M. Calo, T.J.R. Hughes, S. Hulshoff, The role of continuity in residual-based variational multiscale modeling of turbulence, Comput. Mech. 41 (2008) 371–378.
[17] J.A. Cottrell, T.J.R. Hughes, A. Reali, Studies of refinement and continuity in isogeometric structural analysis, Comput. Methods Appl. Mech. Engrg. 196 (2007) 4160–4183.
[18] T. Kloeppel, A. Popp, U. Kuettler, W.A. Wall, Fluid–structure interaction for non-conforming interfaces based on a dual mortar formulation, Comput. Methods Appl. Mech. Engrg. 200 (2011) 3111–3126.
[19] W.K. Liu, Y. Liu, D. Farrell, L. Zhang, X.S. Wang, Y. Fukui, N. Patankar, Y. Zhang, C. Bajaj, J. Lee, J. Hong, X. Chen, H. Hsu, Immersed finite element method and its applications to biological systems, Comput. Methods Appl. Mech. Engrg. 195 (2006) 1722–1749.
[20] W.K. Liu, D.W. Kim, S. Tang, Mathematical foundations of the immersed finite element method, Comput. Mech. 39 (2007) 211–222.
[21] R. Löhner, J.R. Cebral, F.E. Camelli, S. Appanaboyina, J.D. Baum, Eric L. Mestreau, O.A. Soto, Adaptive embedded and immersed unstructured grid techniques, Comput. Methods Appl. Mech. Engrg. 197 (25–28) (2008) 2173–2197. Immersed Boundary Method and Its Extensions.
[22] M.C. Hsu, Y. Bazilevs, V.M. Calo, T.E. Tezduyar, T.J.R. Hughes, Improving stability of stabilized and multiscale formulations in flow simulations at small time steps, Comput. Methods Appl. Mech. Engrg. 199 (2010) 828–840.
[23] O. González, Time integration and discrete Hamiltonian systems, J. Nonlinear Sci. 6 (1996) 449–467.
[24] O. González, Exact energy and momentum conserving algorithms for general models in nonlinear elasticity, Comput. Methods Appl. Mech. Engrg. 190 (2000) 1763–1783.
[25] C.S. Peskin, Flow patterns around heart values: A numerical method, J. Comput. Phys. 10 (1972) 252–271.
[26] C.S. Peskin, Numerical analysis of blood flow in the heart, J. Comput. Phys. 25 (1977) 220–252.
[27] C.S. Peskin, The immersed boundary method, Acta Numer. 11 (2002) 479–517.
[28] J.C. Simo, F. Armero, Geometrically non-linear enhanced strain mixed methods and the method of incompatible modes, Int. J. Numer. Methods Engrg. 33 (1992) 1413–1449.
[29] J.C. Simo, F. Armero, R.L. Taylor, Improved versions of assumed enhanced strain tri-linear elements for 3d finite deformation problems, Comput. Methods Appl. Mech. Engrg. 110 (1993) 359–386.
[30] J.C. Simo, M.S. Rifai, A class of mixed assumed strain methods and the method of incompatible modes, Int. J. Numer. Methods Engrg. 29 (1990) 1595–1638.
[31] L. Tae-Rin, Y. Chang, J. Choi, D.W. Kim, W.K. Liu, Y. Kim, Immersed finite element method for rigid body motions in the incompressible Navier–Stokes flow, Comput. Methods Appl. Mech. Engrg. 197 (2008) 2305–2316.
[32] T.E. Tezduyar, Stabilized finite element formulations for incompressible flow computations, Adv. Appl. Mech. 28 (1992) 1–44.
[33] T.E. Tezduyar, Finite element methods for flow problems with moving boundaries and interfaces, Arch. Comput. Methods Engrg. 8 (2001) 83–130.
[34] T.E. Tezduyar, Y. Osawa, Finite element stabilization parameters computed from element matrices and vectors, Comput. Methods Appl. Mech. Engrg. 190 (2000) 411–430.
[35] H. Wang, J. Chessa, W.K. Liu, T. Belytschko, The immersed/fictitious element method for fluid–structure interaction: volumetric consistency, compressibility and thin memebers, Int. J. Numer. Methods Engrg. 74 (2008) 32–55.
[36] X. Wang, W.K. Liu, Extended immersed boundary method using FEM and RKPM, Comput. Methods Appl. Mech. Engrg. 193 (2004) 1305–1321.

[37] X.S. Wang, L.T. Zhang, W.K. Liu, On computational issues of immersed finite element methods, J. Comput. Phys. 228 (2009) 2535–2551.
[38] C. Wood, A.J. Gil, O. Hassan, J. Bonet, Partitioned block-Gauss–Seidel coupling for dynamic fluid–structure interaction, Comput. Struct. (2008), http://dx.doi.org/10.1016/j.compstruc.2008.08.005.
[39] Y. Bazilevs, V.M. Calo, J.A. Cottrel, T.J.R. Hughes, A. Reali, G. Scovazzi, Variational multiscale residual-based turbulence modeling for large eddy simulation of incompressible flows, Comput. Methods Appl. Mech. Engrg. 197 (2007) 173–201.
[40] Allen R. York II, Deborah Sulsky, Howard L. Schreyer, Fluid-membrane interaction based on the material point method, Int. J. Numer. Methods Engrg. 48 (6) (2000) 901–924.
[41] L. Zhang, A. Gerstenberger, X. Wang, W.K. Liu, Immersed finite element method, Comput. Methods Appl. Mech. Engrg. 193 (2004) 2051–2067.
[42] O.C. Zienkiewicz, R.L. Taylor, P. Nithiarasu, The Finite Element Method for Fluid Dynamics, sixth ed., Butterworth Heinemann, 2005.